Determination of the absolute carrier-envelope phase by angle-resolved photoelectron spectra of Ar by intense circularly polarized few-cycle pulses

Shinichi Fukahori,[1] Toshiaki Ando,[1] Shun Miura,[1] Reika Kanya,[1] Kaoru Yamanouchi,[1,*] Tim Rathje,[2] and Gerhard G. Paulus[2]

[1]*Department of Chemistry, School of Science, The University of Tokyo, 7-3-1 Hongo, Bunkyo-ku, Tokyo 113-0033, Japan*

[2]*Institut für Optik und Quantenelektronik, Friedrich-Schiller-Universität, Max-Wien-Platz 1, 07743 Jena, Germany*

(Received 11 February 2017; published 22 May 2017)

The angle-resolved photoelectron spectra of Ar are recorded using intense circularly polarized near-infrared few-cycle laser pulses, and the effect of the depletion of Ar atoms by the ionization and the effect of the Coulombic potential are examined by the classical trajectory Monte Carlo simulations. On the basis of the comparison between the experimental and theoretical photoelectron spectra, a procedure for estimating the absolute carrier-envelope phase (CEP) of the few-cycle laser pulses interacting with atoms and molecules is proposed. It is confirmed that the absolute CEP can securely be estimated without any numerical calculations once the angular distribution of the yield of photoelectrons having the kinetic energy larger than 30 eV is measured with the peak laser intensity in the range between 1×10^{14} and 5×10^{14} W/cm^2.

DOI: 10.1103/PhysRevA.95.053410

I. INTRODUCTION

Recent advances in ultrashort pulsed laser technology enabled us to generate ultimately short laser pulses whose duration is as short as a few optical cycles [1]. For the characterization of such few-cycle laser pulses, its carrier-envelope phase (CEP), which is conventionally defined as the phase shift of the electric field of light from a cosine-type shape within an ultrashort laser pulse [2], needs to be specified. The CEP dependencies in the attosecond pulse generation [3,4], the high-order harmonic generation [5], and the photoelectron emission [2,6,7] have been examined. It has also been revealed that chemical bond breaking processes by an ultrashort laser pulse are influenced by its CEP [8–12] as well as by its wavelength, pulse duration, and intensity [13–15].

Paulus *et al.* [2] showed that, when atoms are irradiated with linearly polarized few-cycle laser pulses, the direction of the emission of photoelectrons varies depending on the CEP of the laser pulses, and developed an apparatus called the phasemeter. Using the phasemeter, the CEP of few-cycle laser pulses was recorded by taking advantage of the asymmetry of photoelectron emission direction in above-threshold ionization (ATI). Since then, the CEP dependence of the optical responses of atoms and molecules has been an attractive research theme in ultrafast intense field molecular science.

However, it has been a difficult task to determine the absolute CEP of laser pulses employed in experiment, defined as the CEP of the laser pulse at the spatial point where atoms and molecules are irradiated with the laser pulse. Therefore, the absolute CEP has been estimated with the aid of theoretical calculations. For example, in the generation of high-order harmonics, the absolute CEP was determined by the comparison between the experimental and calculated spectra of high-order harmonics even though there was always an ambiguity of $n\pi$ with n being an integer [5,16]. By using the method called attosecond streaking, the absolute CEP can also be extracted [17] by the determination of the wave form of the laser electric field.

In the case of the stereo-ATI measurements [2], the absolute CEP is determined by the assumption that the cutoff energy of the electrons ejected along the laser polarization takes a maximum value when the absolute CEP of the few-cycle laser pulse is around 0.3π. The absolute CEP was also estimated from the CEP-dependent recoil momentum distribution of Ar^{2+} ejected through nonsequential double ionization [18,19], and from the CEP dependence of the mean value of the recoil momentum of $C_2D_2^+$ generated through the photoionization of C_2D_2 [10]. In these studies, the absolute CEP was estimated by a comparison between the experimental results and the theoretical estimates [20,21] obtained by solving Newton's equation of motion for an electron generated after the ionization and/or the electron recollision in an intense linearly polarized laser field. It was reported recently [22] that the absolute CEP of linearly polarized few-cycle laser pulses can be determined by the stereo-ATI measurement with the aid of theoretical calculation in which the three-dimensional time-dependent Schrödinger equation of an H atom is solved numerically.

On the one hand, it has been proposed [6,23–25] that a circularly polarized few-cycle laser pulse can also be used for the determination of absolute CEP. In a circularly polarized few-cycle laser pulse, the direction of the laser electric vector rotates, and consequently, the emitting direction of photoelectrons varies depending on the CEP. It has been shown in the recent theoretical calculations [26,27] based on the strong-field approximation that, in the ionization of an H atom in an intense laser field (5×10^{13} W/cm^2), the distribution of the photoelectron final momentum vectors rotates about the laser propagation axis by the same angles as the rotation angles of the laser polarization vectors in a circularly polarized laser pulse. A similar phenomenon of the rotation of the photoelectron momentum vector distribution was investigated theoretically for the ionization of H_2^+ in a circularly polarized attosecond laser pulse [28], which is the superposition of two-color ultraviolet laser fields. These theoretical studies showed that the absolute CEP can in principle be determined by measuring the angular distribution

*Corresponding author: kaoru@chem.s.u-tokyo.ac.jp

of electrons ejected by a circularly polarized few-cycle laser field.

However, in order to determine experimentally the absolute CEP of an intense circularly polarized few-cycle laser field, it becomes necessary to evaluate quantitatively the variation of the photoelectron yields originated from the two different factors. One is the depletion of neutral atoms by the ionization during the laser pulse [6], and the other is the Coulombic potential between an ejecting electron and the remaining atomic ion, affecting the emitting direction of the photoelectrons, resulting in the Coulomb asymmetry [29–33].

In the present study, we show that the absolute CEP can be determined experimentally by recording the angle-resolved photoelectron spectra of Ar using intense circularly polarized few-cycle pulses. By performing classical trajectory Monte Carlo simulations, we examine the two effects, that is, the effect of the depletion of Ar atoms in the sample volume and the effect of the Coulombic potential between an ejecting electron and Ar^+, and show that the absolute CEP can be estimated without any numerical calculations as long as Ar is used as a sample gas to be ionized and the laser field intensity of the circularly polarized near-infrared (IR) few-cycle laser pulses is in the range between 1×10^{14} and 5×10^{14} W/cm^2.

II. EXPERIMENT

Figure 1 shows the overview of the experimental setup. Linearly polarized femtosecond laser pulses (30 fs, 800 nm, 480 μJ, 5 kHz) generated by a chirped-pulse-amplification Ti:sapphire laser system [34] are introduced into a hollow-core fiber (330 μm inner diameter, 1.5 m long) filled with an Ar gas (~50 kPa) so that their spectral bandwidth was broadened to 280 nm [full width at half maximum (FWHM)] by the self-phase modulation. The blueshift of the central wavelength from 800 to 722 nm can be ascribed to the slight decrease in the refractive index of Ar in the hollow-core fiber associated with the ionization. The negative second- and third-order dispersions were introduced by subsequent multiple reflections at chirped mirrors [35], and the laser pulses passed through a pair of thin-film polarizers [36]. Then, the third-order dispersion was compensated by a fused-silica cell (2.5 mm thickness) containing water [37] whose optical path length was 5 mm. After passing through the cell, the laser pulses were split into two beams by a broadband beam splitter ($R\sim35\%$). One of the two beams is introduced into a phasemeter [38] and the other is introduced into a photoelectron energy analyzer [39]. The second-order dispersion of the two split beams was optimized by a pair of wedged fused-silica plates placed in each of the two beam paths so that few-cycle laser pulses ($\Delta t=4.1$ fs) were obtained. The pulse duration and the spectral phase of the laser pulses were measured by the method called two-dimensional spectral shearing interferometry (2DSI) [40,41]. The pulse energy was reduced and adjusted by selecting the central part of the spatial distribution of the laser pulses by an iris placed in each of the two beam paths. Just before the entrance window (antireflective-coated fused silica, 1 mm thickness) of the photoelectron energy analyzer, a broadband quarter wave plate [42] was placed for generating right-handed circularly polarized pulses.

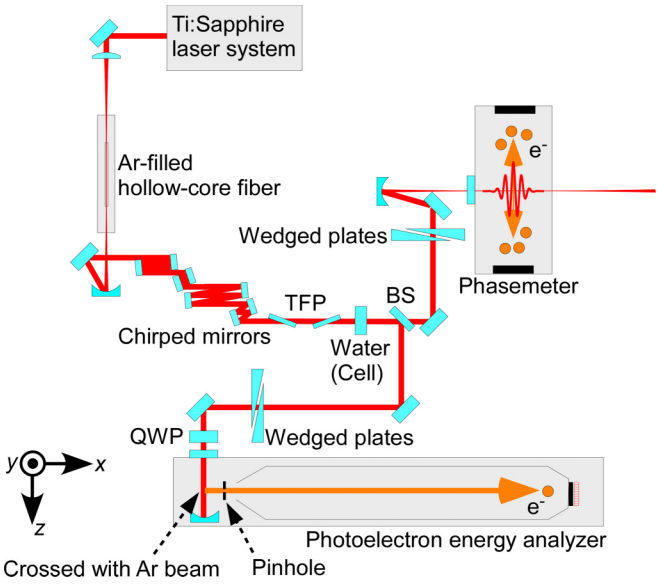

FIG. 1. The schematics of the experimental setup. TFP: thin-film polarizer; BS: beam splitter; QWP: quarter wave plate.

The photoelectron energy analyzer was operated in the transmission mode so that a field-free time-of-flight photoelectron spectrum was recorded. The few-cycle laser pulses were focused by an Ag-coated concave mirror ($f=75$ mm) onto an effusive beam of an Ar gas at right angles. The photoelectrons ejected along the time-of-flight tube were detected by a position sensitive detector [43] composed of two microchannel plates (40 mm diameter) and delay-line anodes placed 1.008 m away from the sample-laser interaction point so that the acceptance angle became $\pm1.2^\circ$. An Al plate (1 mm thickness) with a tapered pinhole (1.0 mm diameter) was installed 25 mm downstream of the sample-laser interaction point towards the detector, preventing stray electrons from hitting the detector. The time origin of the flight time was determined by the signals of the high-order harmonics generated by linearly polarized few-cycle laser pulses, that is, the peak representing the high-order harmonics in the recorded time-of-flight spectrum. The peak laser-field intensity at the focal point was estimated from the pulse energy, the pulse duration, and the focal radius. The focal radius w_0 was defined as the $1/e^2$ radius of the focal spot image of the laser pulses recorded by a charge-coupled device (CCD) camera [44].

The CEP of each laser pulse was measured by the phasemeter [38] in coincidence with the photoelectrons recorded by the photoelectron energy analyzer. In the CEP measurements by the phasemeter, the signal intensities representing the left-right asymmetry [2] of rescattered photoelectrons generated by the linearly polarized few-cycle pulses were recorded for respective laser shots by an eight-bit digitizer [45]. The CEP obtained by the phasemeter is a relative value and needs to be shifted by a constant phase to convert it into the absolute CEP at the sample-laser interaction point in the photoelectron energy analyzer. This constant shift originates from the difference in the total amount of the dispersion of the optical path from the beam splitter to the phasemeter and that from the beam splitter to the photoelectron energy analyzer.

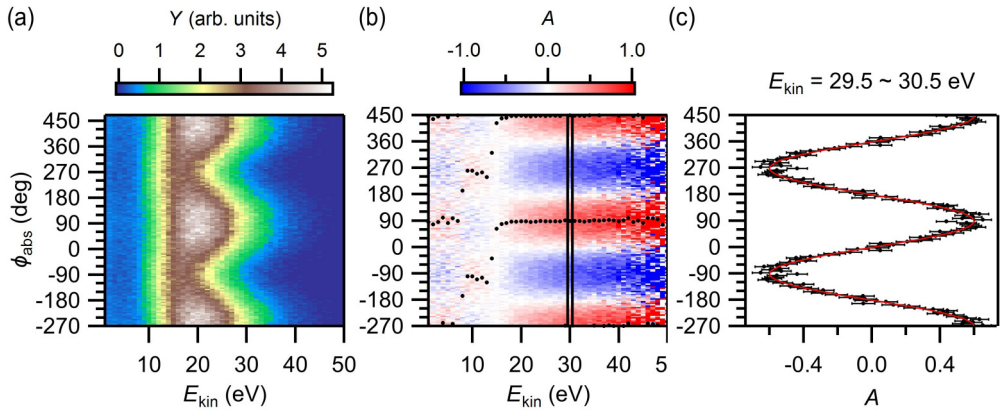

FIG. 2. (a) The experimental CEP-resolved photoelectron spectrum recorded at the peak laser-field intensity of 5.1×10^{14} W/cm^2. (b) The $E_{\rm kin}$-$\phi_{\rm abs}$ asymmetry map constructed from (a). The values of the phase offset (ϕ_0) are plotted with black dots. (c) The asymmetry parameter A in the kinetic energy range (29.5–30.5 eV) between the two vertical lines in (b) plotted as a function of CEP. The red solid curve is the sinusoidal function derived by the least-squares fit to the variation of the asymmetry parameter. The CEP values in these figures are those converted from the relative CEP ($\phi_{\rm rel}$) to the absolute CEP ($\phi_{\rm abs}$). The data in the range of $\pi < \phi_{\rm abs} < 5\pi/2$ are the same as the data in the range of $-\pi < \phi_{\rm abs} < \pi/2$, and the data in the range of $-3\pi/2 < \phi_{\rm abs} < -\pi$ are the same as the data in the range of $\pi/2 < \phi_{\rm abs} < \pi$.

III. RESULTS AND DISCUSSION

A. $E_{\rm kin}$-$\phi_{\rm abs}$ asymmetry map

Figure 2(a) shows the CEP-resolved photoelectron spectrum recorded when the peak laser-field intensity is 5.1×10^{14} W/cm^2 at the focal point. The focal diameter was measured to be $2w_0 = 33.6\,\mu$m. The absolute CEP, $\phi_{\rm abs}$, in Fig. 2 was derived from the relative CEP, $\phi_{\rm rel}$, recorded by the phasemeter after the calibration procedure described later in Sec. III B 4. The signal intensity $Y(E_{\rm kin},\phi_{\rm abs})$ varies depending on the absolute CEP as well as on the photoelectron energy $E_{\rm kin}$. In order to describe the extent of the asymmetry in the signal intensities, we introduce an asymmetry parameter $A(E_{\rm kin},\phi_{\rm abs})$ defined as

$$A(E_{\rm kin},\phi_{\rm abs}) = \frac{Y(E_{\rm kin},\phi_{\rm abs}) - Y(E_{\rm kin},\phi_{\rm abs}+180^\circ)}{Y(E_{\rm kin},\phi_{\rm abs}) + Y(E_{\rm kin},\phi_{\rm abs}+180^\circ)}. \quad (1)$$

The numerical values of the asymmetry parameter $A(E_{\rm kin},\phi_{\rm abs})$ obtained from the CEP-resolved photoelectron spectrum of Fig. 2(a) are plotted as shown in Fig. 2(b), which is hereafter called an $E_{\rm kin}$-$\phi_{\rm abs}$ asymmetry map.

Because the variation of the asymmetry parameter at a fixed value of the photoelectron kinetic energy is represented well by a sinusoidal function of $\phi_{\rm abs}$ as shown in Fig. 2(c), its CEP dependence is fitted to a cosine function of $\phi_{\rm abs}$,

$$A(E_{\rm kin},\phi_{\rm abs}) = A_0(E_{\rm kin})\cos[\phi_{\rm abs} - \phi_0(E_{\rm kin})]. \quad (2)$$

By a least-square analysis, the amplitude $A_0(E_{\rm kin})$ and the phase offset $\phi_0(E_{\rm kin})$ are determined. The phase offset values $\phi_0(E_{\rm kin})$ thus obtained from the experimental data in Fig. 2(a) are plotted as a function of $E_{\rm kin}$ as shown in Fig. 2(b) with black dots, representing the $\phi_{\rm abs}$ value at which the photoelectron yield takes a maximum value within the respective bins of the photoelectron kinetic energy whose width is 1 eV. In the energy range of $E_{\rm kin} > 18$ eV in Fig. 2(b), the phase offset $\phi_0(E_{\rm kin})$ takes almost constant values of $\phi_0(E_{\rm kin}) \sim 90^\circ$. On the other hand, in the energy range of $8\,{\rm eV} < E_{\rm kin} < 13\,{\rm eV}$, $\phi_0(E_{\rm kin})$ takes values of $\phi_0(E_{\rm kin}) \sim -90^\circ$, and, in the lower energy range of $E_{\rm kin} < 6$ eV, the phase offset becomes $\phi_0(E_{\rm kin}) \sim 90^\circ$ again.

B. Classical trajectory Monte Carlo simulation with the lower laser intensity

1. Newton's equation of motion

In order to explain the characteristic variation of the phase offset values obtained above, a classical trajectory Monte Carlo (CTMC) simulation was performed. The laser electric field $\mathbf{E}(t,\phi_{\rm abs})$ is assumed to be represented by a Gaussian pulse given by

$$\mathbf{E}(t,\phi_{\rm abs}) = E_0 \exp\left[-2(\ln 2)\left(\frac{t}{\Delta t}\right)^2\right] \times [\hat{\mathbf{x}}\cos(\omega t+\phi_{\rm abs}) - \hat{\mathbf{y}}\sin(\omega t+\phi_{\rm abs})], \quad (3)$$

where E_0 is the maximum amplitude of the electric field of light, ω is the angular frequency, and $\hat{\mathbf{x}}$ and $\hat{\mathbf{y}}$ are unit vectors along the x and y coordinates in the laboratory fixed coordinate system. The x axis represents the direction towards the microchannel plates from the crossing point between the laser beam and the atomic beam. The $\phi_{\rm abs}$ value defines the direction of the electric-field vector at $t = 0$, when the magnitude of the electric field becomes maximum as depicted in Fig. 3(a).

Under the assumption that the magnitude of the momentum $\mathbf{p}(t) = m_{\rm e}[d\mathbf{r}(t)/dt]$ of an electron generated at $t = t_0$ through tunnel ionization is zero, i.e., $|\mathbf{p}(t=t_0)| = 0$, and that the electron obeys Newton's equation of motion in the laser electric field, the final momentum vector of the electron $\mathbf{p}(t\to\infty)$ is given by

$$\mathbf{p}(t\to\infty) = \int_{t_0}^{\infty} [-e\mathbf{E}(t',\phi_{\rm abs})]dt' = -e\mathbf{A}(t_0,\phi_{\rm abs}), \quad (4)$$

which is antiparallel to the vector potential $\mathbf{A}(t_0,\phi_{\rm abs})$ at the moment of the tunnel ionization, where $\mathbf{r}(t)$ is the position of the electron as a function of t. The photoelectrons will only be detected if their momentum vector $\mathbf{p}(t\to\infty)$ is along the

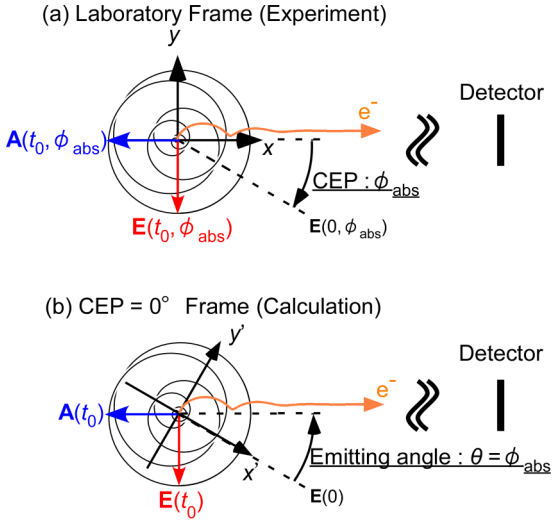

FIG. 3. (a) The ejection direction of a photoelectron in the x-y laboratory frame in which the relative CEP ($\phi_{\rm rel}$) is recorded in the experiment. (b) The ejection direction of a photoelectron expressed in the x'-y' frame in which the emitting angle is simulated by the calculation. The x' axis takes the direction of the maximum amplitude of the circularly polarized light so that CEP becomes 0°.

direction of **x**, and equivalently, the direction of the electric-field vector $\mathbf{E}(t_0,\phi_{\rm abs})$ should be antiparallel to **y**. Therefore, the photoelectron signal intensity is expected to become maximum when $\phi_{\rm abs} = 90°$, that is, when the direction of the electric-field vector at $t_0 = 0$ becomes antiparallel to **y**.

In the experiment, the photoelectron ejected along the x axis is detected whatever the value $\phi_{\rm abs}$ takes, as shown in Fig. 3(a). The variation of $\phi_{\rm abs}$ can also be regarded as the variation of the photoelectron emission angle θ, which is defined as the angle between the direction of the final photoelectron momentum and the direction of the electric-field vector at $t_0 = 0$. Consequently, the $\phi_{\rm abs}$ resolved photoelectron spectrum recorded experimentally becomes identical to the θ resolved photoelectron spectrum evaluated in the new (x',y') coordinate system shown in Fig. 3(b), where the CEP is set to be always 0.

Therefore, the coordinate transformation from the $(x,\ y)$ coordinate system to the new (x',y') coordinate system is performed by the rotation of the angle of $-\phi_{\rm abs}$ about the z axis so that θ becomes equal to $\phi_{\rm abs}$. Within the new (x',y') coordinate system, the electric-field vector of Eq. (3) is expressed as a function of t as

$$\mathbf{E}(t) = E_0 \exp\left[-2(\ln 2)\left(\frac{t}{\Delta t}\right)^2\right](\hat{\mathbf{x}}'\cos\omega t - \hat{\mathbf{y}}'\sin\omega t). \quad (5)$$

When $t_0 = 0$, the direction of the laser electric field $\mathbf{E}(t_0 = 0)$ is along the x' axis and the direction of the vector potential $\mathbf{A}(t_0 = 0)$ is antiparallel to the y' axis, along which a photoelectron is ejected. Figure 4(a) shows a variation of the kinetic energy $E_{\rm kin}$ and the ejection angle θ of a photoelectron obtained by solving Eq. (4), in which the time t_0 is varied in the range of $-1.75T < t_0 < 1.75T$, where T is the period of the optical cycle.

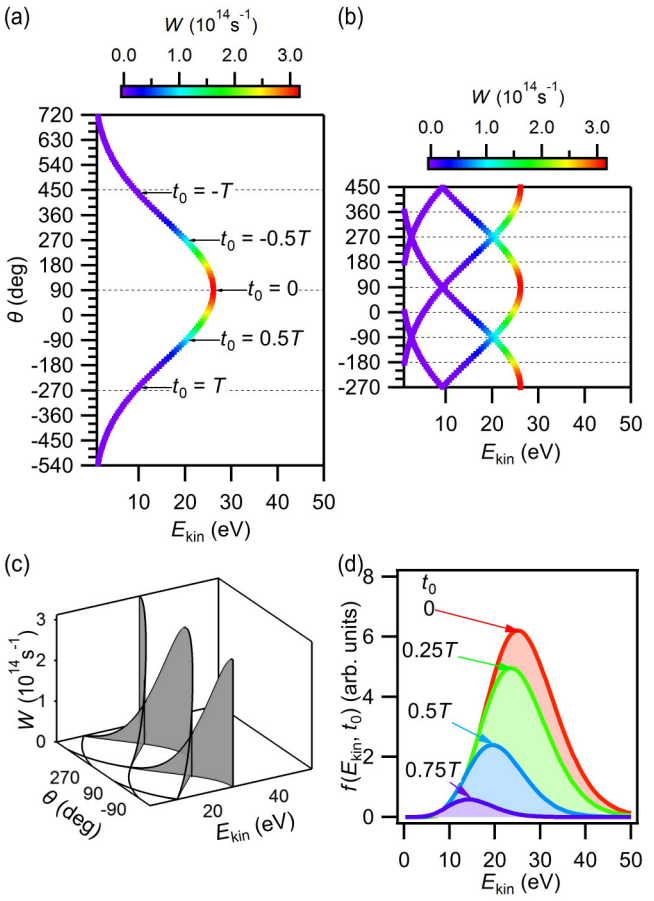

FIG. 4. (a) The $E_{\rm kin}$-θ plot for the ionization rate W, represented by the color scale, obtained by solving Newton's equation of motion of a photoelectron in the laser field whose peak intensity is 5.1×10^{14} W/cm^2. Neither the effect of the depletion of neutral Ar nor the effect of the Coulombic potential of Ar^+ is taken into account. The values of the time of tunneling t_0 are also shown. (b) The folded $E_{\rm kin}$-θ plot in which the five angle ranges of (a) are folded into a 2π angle range: (i) $-3\pi < \theta \leqslant -5\pi/2$, (ii) $-5\pi/2 < \theta \leqslant -\pi/2$, (iii) $-\pi/2 < \theta \leqslant 3\pi/2$, (iv) $3\pi/2 < \theta \leqslant 7\pi/2$, and (v) $7\pi/2 < \theta \leqslant 4\pi$. (c) The 3D representation of (b). (d) The kinetic-energy distribution $f(E_{\rm kin},t_0)$ derived by the initial transverse momentum distribution at the four different values of the time of tunneling: $t_0 = 0$ (red), $0.25T$ (green), $0.5T$ (blue), and $0.75T$ (purple).

The color scale represents the tunneling ionization rate $W(t_0)$ of an electron occupying initially the $3p$ orbital of Ar, which was estimated by the Ammosov-Delone-Krainov (ADK) theory [46,47] as

$$W(t_0) = \frac{I_{\rm p}}{\hbar}\frac{2^{2n^*}}{n^*\Gamma(n^*+l^*+1)\Gamma(n^*-l^*)} \times \frac{2l+1}{2^{|m|}(|m|)!}\frac{(l+|m|)!}{(l-|m|)!}\left(\frac{2\sqrt{8m_{\rm e}I_{\rm p}^{\,3}}}{\hbar e|\mathbf{E}(t_0)|}\right)^{2n^*-|m|-1} \times \exp\left(-\frac{2\sqrt{8m_{\rm e}I_{\rm p}^{\,3}}}{3\hbar e|\mathbf{E}(t_0)|}\right), \quad (6)$$

where I_p is the ionization energy, $n^* = [e^2/(4\pi\varepsilon_0\hbar)]\sqrt{m_e/(2I_p)}$ is the effective principal quantum number, $l^* = n^* - 1$ is the effective angular momentum quantum number, l is the angular momentum quantum number, and m is the magnetic quantum number, where the quantization axis is set to be along the laser polarization axis at $t = t_0$. In the calculation, $I_p = 15.76\,\text{eV}$ and $l = 1$ were adopted, and m was set to be $m = 0$ because the contribution from $m = \pm 1$ is found to be one order of magnitude smaller than $m = 0$. In the following, we will refer to the two-dimensional curve of Fig. 4(a), representing the ionization rate as a function of E_{kin} and θ, as the E_{kin}-θ plot.

Because the direction of the laser field rotates with the period of T, the emission angle of the photoelectrons also rotates three to four times in the range of $-1.75T < t_0 < 1.75T$. In other words, the electrons are ejected in the same angular direction at least three times. Therefore, in order to simulate the angle-resolved photoelectron spectrum, the contributions from the five angle ranges of (i) $-3\pi < \theta \leqslant -5\pi/2$, (ii) $-5\pi/2 < \theta \leqslant -\pi/2$, (iii) $-\pi/2 < \theta \leqslant 3\pi/2$, (iv) $3\pi/2 < \theta \leqslant 7\pi/2$, and (v) $7\pi/2 < \theta \leqslant 4\pi$ need to be added. After folding the contributions from these five angle ranges into a 2π angle range, Fig. 4(b) is obtained, which is called the folded E_{kin}-θ plot. In order to enhance the visibility of the periodicity, the data are plotted over 4π, and in order to emphasize the meaning of the folded E_{kin}-θ plot, its three-dimensional (3D) representation is shown in Fig. 4(c). As shown in Figs. 4(a) and 4(b), both the kinetic energy of a photoelectron and the ionization rate become maximum when the electron ejection angle θ becomes 90°. It should be noted that the emission angle of a photoelectron can be determined uniquely once the time of the tunneling is given [48]. Specifically the time of tunneling $t_0 = 0$ corresponds to the photoelectron emission angle of $\theta = 90°$.

2. *Initial transverse momentum distribution*

In order to simulate the experimental photoelectron energy distribution, the initial transverse momentum $p_\perp$, which is parallel to the vector potential $\mathbf{A}(t_0)$ at the moment of the tunneling, needs to be taken into account. The distribution of the photoelectron energy is assumed to originate from the distribution of $p_\perp$, and the initial momentum perpendicular to the vector potential $\mathbf{A}(t_0)$ at the moment of the tunneling is assumed to be zero in the simulation below. In the present experimental configuration, the acceptance angle of photoelectrons is ±1.2°. Therefore, only the photoelectrons whose momentum p_z along the z axis is sufficiently small can be detected, and the motion of photoelectrons along the z axis is also neglected in the calculations below.

According to the ADK theory [49], the distribution of $p_\perp$ at $t = t_0$ is given by

$$w(p_\perp)dp_\perp = \sqrt{\frac{1}{\pi\hbar e|\mathbf{E}(t_0)|}\sqrt{\frac{2I_p}{m_e}}} \times \exp\left(-\frac{1}{\hbar e|\mathbf{E}(t_0)|}\sqrt{\frac{2I_p}{m_e}}{p_\perp}^2\right)dp_\perp. \quad (7)$$

When numerical values of $p_\perp$ and t_0 are given, the final momentum vector $\mathbf{p}(t \to \infty)$ of a photoelectron in a laser field is obtained by solving Newton's equation of motion,

$$\mathbf{p}(t \to \infty) = p_\perp \hat{\mathbf{e}}_\perp(t_0) + \int_{t_0}^{\infty} [-e\mathbf{E}(t')]dt', \quad (8)$$

where $\hat{\mathbf{e}}_\perp(t_0)$ is a unit vector perpendicular to $\mathbf{E}(t_0)$. At $t_0 = 0$, the vector potential $\mathbf{A}(t_0)$ is perpendicular to $\mathbf{E}(t_0)$, and is antiparallel to $\hat{\mathbf{e}}_\perp(t_0)$. However, it should be noted that $\mathbf{A}(t_0)$ becomes only approximately antiparallel to $\hat{\mathbf{e}}_\perp(t_0)$ in a few-cycle laser pulse when $t_0 \neq 0$.

Using the initial transverse momentum $p_\perp$, the kinetic energy of the photoelectron tunneling at $t = t_0$ is given by $E_{\text{kin}} = [p_\perp + e|\mathbf{A}(t_0)|]^2/(2m_e)$ by assuming that $\mathbf{A}(t_0)$ is antiparallel to $\hat{\mathbf{e}}_\perp(t_0)$. Therefore, the initial transverse momenta are given by

$$p_{\perp+} = -e|\mathbf{A}(t_0)| + \sqrt{2m_e E_{\text{kin}}}, \quad (9)$$

when $p_\perp$ is antiparallel to $\mathbf{A}(t_0)$, and

$$p_{\perp-} = -e|\mathbf{A}(t_0)| - \sqrt{2m_e E_{\text{kin}}}, \quad (10)$$

when $p_\perp$ is parallel to $\mathbf{A}(t_0)$. Because the absolute value of $p_{\perp-}$ is much larger than $|p_{\perp+}|$, i.e., $|p_{\perp-}| \gg |p_{\perp+}|$ under the present conditions, the initial momentum distribution at $p_{\perp-}$, i.e., $w(p_{\perp-})$, is much smaller than that at $p_{\perp+}$. Therefore, the kinetic-energy distribution of the photoelectrons tunneling at $t = t_0$ can be given approximately by the distribution originating from $p_{\perp+}$ as

$$f(E_{\text{kin}}, t_0)dE_{\text{kin}}dt_0 = W(t_0)\tilde{w}(p_{\perp+})dE_{\text{kin}}dt_0, \quad (11)$$

where $\tilde{w}(p_\perp)$ is a scaled initial transverse momentum distribution defined using $w(p_\perp)$, Eq. (7), as

$$\tilde{w}(p_\perp) = w(p_\perp)\sqrt{\frac{m_e}{2E_{\text{kin}}}}. \quad (12)$$

Figure 4(d) shows the kinetic-energy distributions Eq. (11) at $t_0 = 0.25T, 0.5T$, and $0.75T$, corresponding to the distribution at $\theta = 90°, 2°, -85°$, and $-173°$, respectively. It should be noted that the emitting angles at $t_0 = 0.25T, 0.5T$, and $0.75T$ become $\theta = 0°, -90°$, and $-180°$, as long as the pulse duration is sufficiently long so that $\mathbf{A}(t_0)$ is antiparallel to $\hat{\mathbf{e}}_\perp(t_0)$. The angle-resolved photoelectron spectrum synthesized by the trajectory calculation is shown in Fig. 5(a), and can be regarded as the convolution of the folded E_{kin}-θ plot Fig. 4(b) with the convolution function of Eq. (11) shown in Fig. 4(d). The asymmetry parameter obtained from Fig. 5(a) is shown in Fig. 5(b), which is called an E_{kin}-θ asymmetry map. The resultant phase offset ϕ_0 values are plotted with black dots in Fig. 5(b).

In the kinetic energy ranges of $E_{\text{kin}} > 19.5\,\text{eV}$ and $4.5\,\text{eV} < E_{\text{kin}} < 19.5\,\text{eV}$, the phase offset values are found to take constant values of $\phi_0 = 90°$ and $\phi_0 = -90°$, respectively. The constant phase offset of 90° can be ascribed to the fact that the electron yield takes a maximum value at around $t_0 = 0$ as shown in Figs. 4(b) and 4(c), and can be used for the determination of the absolute CEP by the comparison with

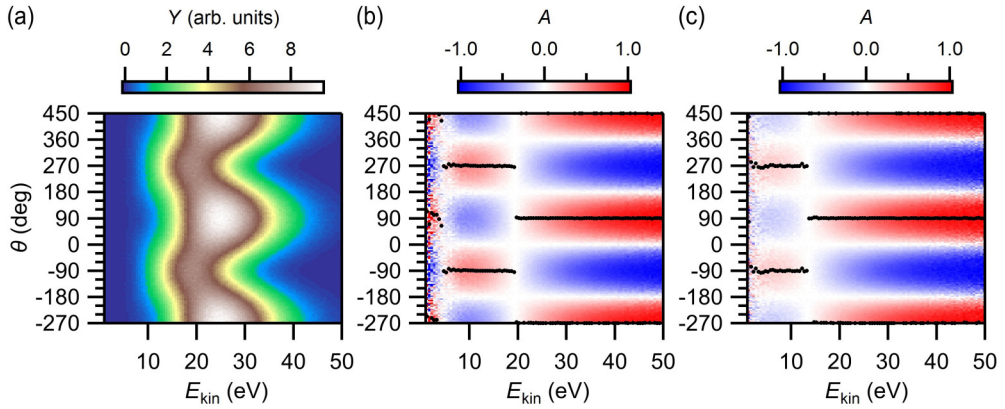

FIG. 5. The results of the CTMC simulations obtained at the peak laser intensity of 5.1×10^{14} W/cm^2. Neither the effect of the depletion of neutral Ar nor the effect of the Coulombic potential of Ar^+ is taken into account. (a) The angle-resolved photoelectron spectrum obtained when the focal averaging effect is neglected. (b) The E_{kin}-θ asymmetry map constructed from (a). (c) The E_{kin}-θ asymmetry map obtained when the focal averaging is taken into account. In (b) and (c), the values of the phase offset (ϕ_0) are plotted with black dots.

the experimental result. In addition, the phase offset of -90° can be ascribed to the crossing at $(E_{kin},\theta) = (20\,\text{eV}, -90^\circ)$, where a relatively large electron yield is expected because the electrons whose momentum is $(E_{kin},\theta) = (20\,\text{eV}, -90^\circ)$ are produced twice at $t_0 = 0.513T$ and $-0.513T$, as shown in Figs. 4(b) and 4(c).

3. Focal averaging effect

In order to simulate the angle-resolved photoelectron spectra, the distribution of the spatial points where a photoelectron is generated also needs to be taken into account. The details of the simulation in which the focal averaging effect is included are described in Appendix A. The synthesized E_{kin}-θ asymmetry map is shown in Fig. 5(c), where the resultant phase offset ϕ_0 values are plotted with black dots. In the kinetic energy ranges of $E_{kin} > 13.5\,\text{eV}$ and $E_{kin} < 13.5\,\text{eV}$, the phase offset values are found to take constant values of $\phi_0 = 90^\circ$ and $\phi_0 = -90^\circ$, respectively. By the focal averaging, the maximum photoelectron energy below which the phase offset takes a value of -90° is changed from 19.5 eV in Fig. 5(b) to 13.5 eV in Fig. 5(c). In the following simulations of the angle-resolved photoelectron spectrum, the focal averaging effect is always taken into account.

4. Determination of absolute CEP by comparison between experiment and simulation

It is found that both the observed E_{kin}-ϕ_{abs} asymmetry map in Fig. 2(b) and the synthesized asymmetry map in Fig. 5(c) exhibit the ridge structure whose ridge positions take almost constant CEP values in the electron kinetic-energy region higher than 30 eV. The CTMC simulation above shows that the phase offset in the high-energy range takes the value of $\phi_0 = 90^\circ$. Therefore, the absolute CEP, ϕ_{abs}, can be determined from the relative CEP, ϕ_{rel}, at which the experimental asymmetry parameter becomes maximum in the high electron kinetic-energy range, by shifting the CEP so that the phase offset becomes $\phi_0 = 90^\circ$.

C. Effects of stray electron, depletion of Ar atoms, and Coulomb potential

1. Stray electron

It is found that the distribution of the experimental asymmetry parameter in Fig. 2(b) and the synthesized distribution in Fig. 5(c) exhibit substantial discrepancies in the low kinetic-energy region of $E_{kin} < 6\,\text{eV}$. In the simulation, the phase offset in the range of $E_{kin} < 6\,\text{eV}$ takes a value of $\phi_0 = -90^\circ$ while the experimental phase offset in the same energy range is $\phi_0 = 90^\circ$. When the Al plate with the tapered pinhole introduced for blocking stray electrons was removed, it was found that the yield of electrons whose kinetic energy is below 6 eV significantly increases, indicating that these low-energy electrons are stray electrons. Therefore, in the following sections, the photoelectrons appearing in the low kinetic-energy region below 6 eV will not be used for the estimation of ϕ_{abs}. These low-energy stray electrons are considered to be generated when photoelectrons ejected with the higher kinetic energy hit the cylindrical electrodes in the photoelectron energy analyzer.

2. Effect of depletion of Ar atom

As was discussed previously on the basis of theoretical calculations [6], the depletion of a sample gas by an intense circularly polarized few-cycle laser pulse needs to be taken into account when determining the CEP. When depletion occurs, the effective ADK rate $W_{eff}(t_0)$ can be described by subtracting the contribution from the ionization of Ar in the earlier part of the laser pulse until $t = t_0$ as

$$W_{\text{eff}}(t_0) = \left(1 - \int_{-\infty}^{t_0} W_{\text{eff}}(t)dt\right) W(t_0) = [1 - P(t_0)]W(t_0), \tag{13}$$

where $W(t)$ is given by Eq. (6) and the integrated ionization probability until t_0 is given by

$$P(t_0) = \int_{-\infty}^{t_0} W_{\text{eff}}(t)dt. \tag{14}$$

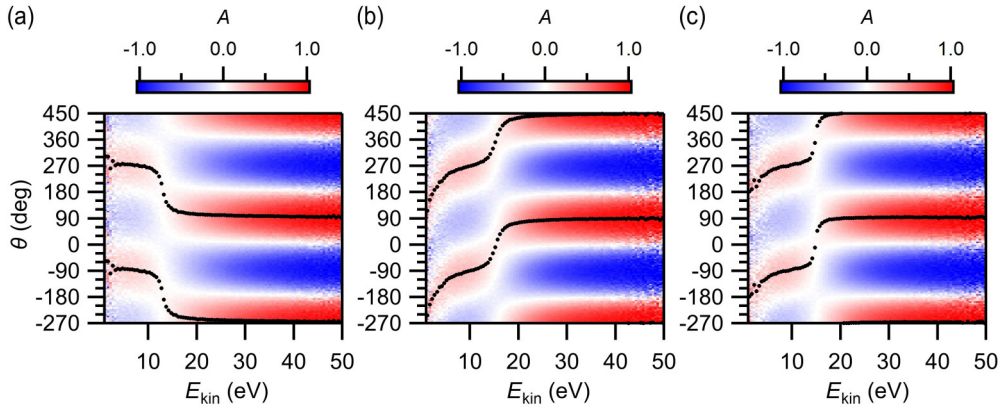

FIG. 6. The $E_{\rm kin}$-θ asymmetry maps obtained by the CTMC simulations when the peak laser intensity is 5.1×10^{14} W/cm^2. The values of the phase offset (ϕ_0) are plotted with black dots. (a) Only the effect of the depletion of neutral Ar is taken into account. (b) Only the effect of the Coulomb potential of Ar^+ is taken into account. (c) Both of the two effects are taken into account.

By solving Eq. (13), the ionization probability can be derived as

$$P(t_0) = 1 - \exp\left[-\int_{-\infty}^{t_0} W(t)dt\right]. \quad (15)$$

When this depletion effect is taken into account, the $E_{\rm kin}$-θ asymmetry map in Fig. 5(c) is converted into Fig. 6(a). In contrast to the phase offset obtained from Fig. 5(c), in which the depletion effect is neglected, the phase offset in Fig. 6(a) decreases as $E_{\rm kin}$ increases with the different negative slopes in the two regions, 12 eV $< E_{\rm kin} <$ 15 eV and $E_{\rm kin} >$ 20 eV.

In the range of 12 eV $< E_{\rm kin} <$ 15 eV, the phase offset exhibits a sharp drop. Because the depletion of Ar atom occurs in the earlier part of the laser pulse, the time of tunneling at which the effective ionization rate becomes maximum appears earlier, that is, t_0 becomes $t_0 < 0$. Consequently, as shown in the folded $E_{\rm kin}$-θ plot, Fig. 9(e) in Appendix B, $E_{\rm kin}$ at which the electron yield takes a maximum value becomes smaller than that obtained when the depletion is not taken into account, and the corresponding θ value becomes larger. The negative steep slope at the transition region in Fig. 6(a) is ascribed to the decrease in the emitting angle associated with the increase in the electron kinetic energy shown in Fig. 9(e).

On the other hand, in the range of $E_{\rm kin} >$ 20 eV, the phase offset decreases only slightly as $E_{\rm kin}$ increases. The higher energy photoelectrons are considered to be originated from the tail part of the kinetic energy distribution $f_{\rm eff}(E_{\rm kin},t_0)$,

$$f_{\rm eff}(E_{\rm kin},t_0)dE_{\rm kin}dt_0 = W_{\rm eff}(t_0)\tilde{w}(p_{\perp+})dE_{\rm kin}dt_0, \quad (16)$$

derived by replacing $W(t_0)$ in Eq. (11) with $W_{\rm eff}(t_0)$. When $t_0 = 0$, the magnitude of the electric field $|\mathbf{E}(t_0)|$ takes the maximum value, and consequently, (i) the width of the distribution $w(p_\perp)$ given by Eq. (7) becomes maximum and (ii) the $E_{\rm kin}$ value in the folded $E_{\rm kin}$-θ plot becomes the largest. It is true that the effective ionization rate $W_{\rm eff}(t_0)$ in the range of $-0.17T < t_0 < 0$ is larger than $W_{\rm eff}(t_0 = 0)$. However, even at the maximum value of $W_{\rm eff}(t_0)$ taken at $t_0 = -0.085T$ and $\theta = 120^\circ$ shown in the folded $E_{\rm kin}$-θ plot, $W_{\rm eff}(t_0)$ is larger than $W_{\rm eff}(t_0 = 0)$ only by 3%, and therefore, because of the two effects above extending the contribution at $t_0 = 0$ to the larger kinetic-energy region, the behavior of the dependence of the ionization yield on θ in the large kinetic-energy region is governed by the contribution from $t_0 = 0$. As shown in Fig. 6(a), the $E_{\rm kin}$ dependence of the phase offset becomes almost flat when $E_{\rm kin} >$ 45 eV, and the phase offset converged to $\phi_0 \sim 95^\circ$. It can be said that, as long as the laser intensity is 5.1×10^{14} W/cm^2, ϕ_0 becomes only slightly larger than 90° by the depletion effect in the electron kinetic-energy region above 45 eV.

3. *Effect of Coulombic potential*

The effect of the Coulombic potential of Ar^+ appearing in the angle-resolved photoelectron spectrum can be examined by solving Newton's equation of motion,

$$\mathbf{p}(t\to\infty) = p_\perp \hat{\mathbf{e}}_\perp(t_0) + \int_{t_0}^{\infty}\left[-e\mathbf{E}(t') - \frac{e^2}{4\pi\varepsilon_0|\mathbf{r}(t')|^3}\mathbf{r}(t')\right]dt'. \quad (17)$$

In Eq. (17), the initial momentum $p_\perp$ is determined from the initial momentum distribution, Eq. (7), and the initial position of an electron $\mathbf{r}(t_0)$ is set to be

$$\mathbf{r}(t_0) = -\frac{I_{\rm p} + \sqrt{{I_{\rm p}}^2 - \left[\frac{e^3}{\pi\varepsilon_0} - 2\hbar e\sqrt{\frac{2I_{\rm p}}{m_{\rm e}}}(1+|m|)\right]|\mathbf{E}(t_0)|}}{2e|\mathbf{E}(t_0)|} \times \frac{\mathbf{E}(t_0)}{|\mathbf{E}(t_0)|}, \quad (18)$$

which is called the tunnel exit. The tunnel exit is derived in a parabolic coordinate system [50,51], assuming that the Coulombic potential of Ar^+ modified by the laser field at the tunnel exit takes the same value as the ionization energy $-I_{\rm p}$.

By taking into account the Coulombic potential, the $E_{\rm kin}$-θ asymmetry map Fig. 5(c) is converted into Fig. 6(b). As shown in Fig. 6(b), the phase offset increases as $E_{\rm kin}$ increases. In Fig. 3, the photoelectron is ejected towards the direction antiparallel to the electric field $\mathbf{E}(t_0)$ just after the tunneling. However, its ejection direction is bent by the laser field, and consequently, its final momentum becomes antiparallel to the vector potential $\mathbf{A}(t_0)$. When the attractive force acting between the ejecting electron and Ar^+ is taken into account, the ejection direction is further bent and the electron emitting angle becomes shifted towards the $-\theta$ direction. Therefore, the

direction of the shift of the phase offset from $\phi_0 = 90^\circ$ induced by the Coulombic potential is opposite to the depletion effect.

The photoelectrons having a large initial momentum along the direction antiparallel to $\mathbf{A}(t_0)$ can escape rapidly from the spatial domain close to the Ar^+ core to the spatial domain where the Coulombic field is much smaller than the laser electric field. Therefore, as shown in Fig. 6(b), the effect of the Coulombic potential is small in the high kinetic-energy region. In the electron kinetic-energy region of $E_{kin} > 45$ eV, the phase offset takes an almost constant value of $\phi_0 \sim 88^\circ$.

When both the depletion of neutral Ar and the Coulombic effect are taken into account, the E_{kin}-θ asymmetry map Fig. 5(c) is converted into Fig. 6(c). The phase offset exhibits the small positive slope in the range of $E_{kin} < 20$ eV. However, the phase offset takes an almost constant value of $\phi_0 \sim 90^\circ$ in the range of $E_{kin} > 30$ eV.

Therefore, without any numerical calculation, the absolute CEP of circularly polarized pulses can be determined so that the experimental phase offset where the ridge of the E_{kin}-ϕ_{abs} asymmetry map is located in the range of $E_{kin} > 30$ eV becomes $\phi_0 = 90^\circ$.

D. Photoelectron angular distribution at higher laser intensity

Figure 7(a) shows the CEP-resolved photoelectron spectrum recorded when the peak laser-field intensity is 1.2×10^{15} W/cm^2 at the focal point. In Fig. 7(a), the absolute CEP ϕ_{abs} has already been calibrated based on the experimental results obtained for the laser intensity of 5.1×10^{14} W/cm^2. The focal diameter was measured to be $2w_0 = 28.9\,\mu$m. The E_{kin}-ϕ_{abs} asymmetry map constructed from Fig. 7(a) and the phase offset are shown in Fig. 7(b). The phase offset at $E_{kin} \sim 20$ eV takes the values of $\phi_0 \sim -70^\circ$, but it decreases as E_{kin} increases monotonically as shown in Fig. 7(b), exhibiting a marked contrast with Fig. 2(b) obtained at the lower laser intensity.

In Fig. 8, the results of the CTMC simulations performed with the laser intensity of 1.2×10^{15} W/cm^2 are shown. When both the depletion effect and the Coulombic potential effect are taken into account, the angle-resolved photoelectron spectrum is obtained as in Fig. 8(a). The E_{kin}-θ asymmetry map constructed from Fig. 8(a) is shown in Fig. 8(b). The effective ionization rate at $t_0 = 0$ becomes three orders of magnitude smaller by taking into account the depletion effect. That is, neutral Ar atoms are depleted almost completely before the laser field intensity becomes maximum at $t_0 = 0$. Because of this depletion effect, the emitting angle at which the effective ionization rate takes a maximum value in the folded E_{kin}-θ plot, Fig. 10(m) in Appendix C, becomes as large as $\theta = 310^\circ$.

Correspondingly, in Fig. 8(b), the phase offset decreases as E_{kin} increases in the range of $E_{kin} > 30$ eV. The decrease in the phase offset in the experimental result shown in Fig. 7(b) is qualitatively reproduced. However, in Fig. 8(b), the calculated phase offset in the energy range of $E_{kin} > 80$ eV becomes $\phi_0 \sim 180^\circ$, while, in Fig. 7(b), the experimental phase offset becomes $\phi_0 \sim 120^\circ$.

Furthermore, in the calculated angle-resolved photoelectron spectrum, Fig. 8(a), the angle θ at which the photoelectron yield becomes maximum decreases as E_{kin} increases in the range of 25 eV $< E_{kin} <$ 45 eV, similarly to the experimental CEP-resolved photoelectron spectrum Fig. 7(a). However, in Fig. 8(a), the calculated electron energy at which the

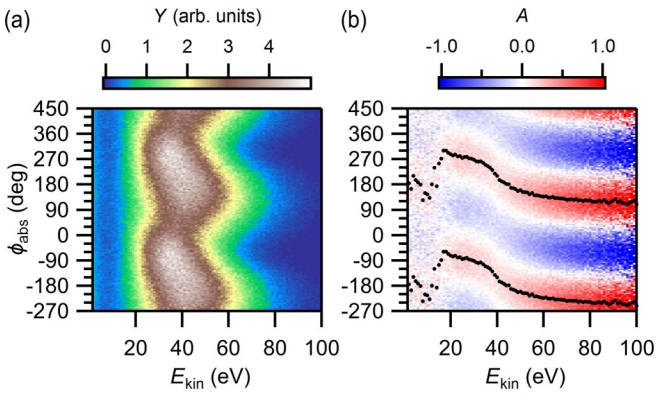

FIG. 7. (a) The experimental CEP-resolved photoelectron spectrum recorded at the peak laser-field intensity of 1.2×10^{15} W/cm^2. (b) The E_{kin}-ϕ_{abs} asymmetry map constructed from (a). The values of the phase offset (ϕ_0) are plotted with black dots. The CEP values in (a) and (b) are those converted from the relative CEP (ϕ_{rel}) to the absolute CEP (ϕ_{abs}).

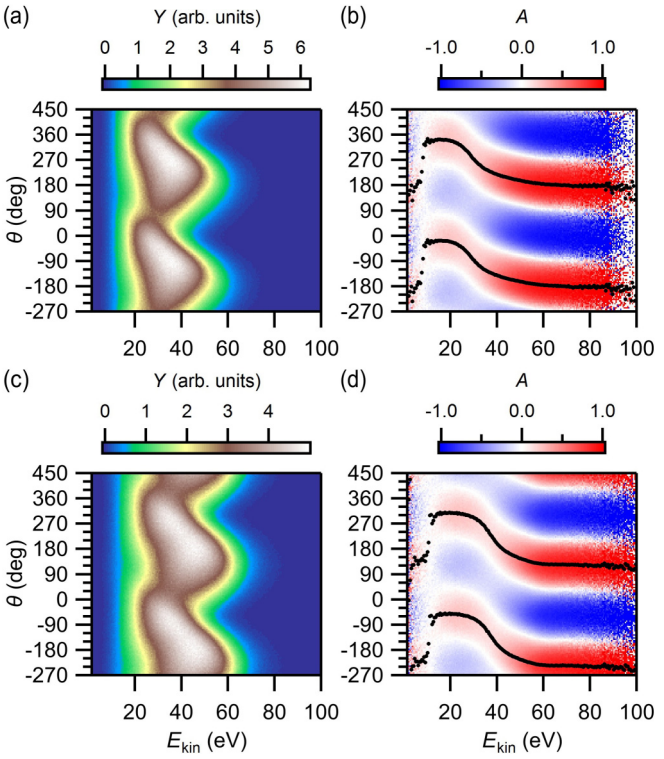

FIG. 8. The results of the CTMC simulations obtained when the peak laser intensity is 1.2×10^{15} W/cm^2. Both the effect of the depletion of neutral Ar and the effect of the Coulombic potential of Ar^+ are taken into account. (a) The angle-resolved photoelectron spectrum. (b) The E_{kin}-θ asymmetry map constructed from (a). (c) The angle-resolved photoelectron spectrum obtained when the ionization rate W_{eff} is calculated using the scaled ADK rate with the scale factor of 0.27. (d) The E_{kin}-θ asymmetry map constructed from (c). In (b) and (d), the values of the phase offset (ϕ_0) are plotted with black dots.

electron yield becomes maximum is $E_{\rm kin} \sim 31$ eV while, in Fig. 7(a), the experimental kinetic energy of electrons at which the electron yield becomes maximum is $E_{\rm kin} \sim 38$ eV. The quantitative discrepancies between the experimental results shown in Figs. 7(a) and 7(b) and the simulated results shown in Figs. 8(a) and 8(b) show that it is not straightforward to estimate the absolute CEP when the laser intensity is as high as 1.2×10^{15} W/cm^2, in contrast to the lower laser intensity case where the phase offset in the high kinetic-energy region can be considered to be $\phi_0 \sim 90^\circ$.

In order to estimate the depletion effect quantitatively, the ionization rate needs to be evaluated with high accuracy. Because the ADK theory is based on the single active electron approximation, the ionization rate of a multielectron atom obtained by the ADK theory is expected to be overestimated due to the screening effect [52]. When the ADK rate is multiplied by a factor of 0.27, Figs. 8(a) and 8(b) are converted into Figs. 8(c) and 8(d), respectively. Both the phase offset and the electron kinetic energies obtained by the simulation are in good agreement with the experimental values, suggesting that the absolute ionization rate can be estimated by adopting the scaling factor of 0.27 for the ADK ionization rate. Therefore, once an appropriate scaling factor for the ADK ionization rate is obtained, the absolute CEP can be estimated even when the laser field intensity is high so that the depletion effect becomes significant.

E. Procedure for the determination of absolute CEP

In order to examine the laser field intensity range in which the phase offset in the sufficiently large electron kinetic-energy range can be regarded as $\phi_0 \sim 90^\circ$, the CTMC simulations described above in Secs. III B and III C were performed in the laser field intensity range of 1×10^{14}–1×10^{15} W/cm^2. Below the lower bound of this intensity range, 1×10^{14} W/cm^2, ionization is not regarded as that proceeding through the tunneling, because the Keldysh parameter [53] takes a value in the range of $\gamma > 1$. In the simulations, the focal diameter of $2w_0 = 30\,\mu$m was commonly adopted in the evaluation of the focal averaging effect. It was revealed that, as long as the peak laser field intensity is in the range between 1×10^{14} and 5×10^{14} W/cm^2, the phase offset in the high-energy range takes a constant value between $\phi_0 = 88^\circ$ and $\phi_0 = 93^\circ$.

On the other hand, when the peak laser field intensity is 6×10^{14} W/cm^2 or higher, the depletion effect becomes significant and the phase offset in the high kinetic-energy range increases and deviates significantly from 90°. The extent of the deviation was found to increase as the peak laser field intensity increases. For example, when the peak laser field intensity is 8×10^{14} W/cm^2, the phase offset becomes $\phi_0 = 124^\circ$ in the range of $E_{\rm kin} \sim 60$ eV, and, when the peak laser intensity is 1×10^{15} W/cm^2, the phase offset increases further to $\phi_0 = 152^\circ$ in the range of $E_{\rm kin} \sim 60$ eV.

Therefore, in order to have a constant ridge structure, representing the phase offset of $\phi_0 \sim 90^\circ$ in the high electron kinetic-energy region in the $E_{\rm kin}$-θ asymmetry map of the angular distribution of the electron yield, the peak laser field intensity should be in the range between 1×10^{14} and 5×10^{14} W/cm^2. As long as this laser field condition is fulfilled, the determination of the absolute CEP can be achieved without performing numerical simulations. When the scaling factor of 0.27 for the ADK ionization rate is adopted in the simulation, the constant ridge structure appearing at the phase offset of $\phi_0 \sim 90^\circ$ was found to be realized for the peak laser field intensity up to 6×10^{14} W/cm^2.

This method can also be applied to a few-cycle laser pulse in the longer wavelength region such as in the mid-IR region. When the wavelength becomes longer, the tunneling model can be applied at the weaker light field intensity. Therefore, the lower bound of the light field intensity with which this method could work becomes lower than in the near-IR region. On the other hand, the depletion effect becomes larger as long as the peak laser intensity is the same, which means that the upper bound of the light field intensity with which this method could work becomes lower than in the near-IR region. This means that this method can also be used in the mid-IR range as long as the light field intensity fulfills these requirements. It should be noted that, in the mid-IR region, the Coulombic potential effect may also be negligible in the high kinetic-energy range, because the initial transverse momentum distribution does not depend on the wavelength of the laser field. In addition, the Coulombic potential effect is expected to be smaller in the mid-IR region than in the near-IR region, because the electron momentum gained from the laser field becomes larger in the mid-IR region at the same laser-field intensity.

IV. CONCLUSION

Angle-resolved photoelectron spectra of Ar were recorded using circularly polarized near-IR intense few-cycle pulses ($\Delta t = 4.1$ fs, $\lambda = 722$ nm) at the two peak laser field intensities of 5.1×10^{14} and 1.2×10^{15} W/cm^2. When the peak laser field intensity was 5.1×10^{14} W/cm^2, the $E_{\rm kin}$-$\phi_{\rm abs}$ asymmetry map constructed from the experimental angle-resolved photoelectron spectrum showed that a ridge structure having an almost constant phase offset extends towards the larger electron kinetic-energy region above 30 eV.

The CTMC simulations of photoelectrons were performed by adopting the ADK ionization rate. The resulting folded $E_{\rm kin}$-θ plot was converted into the angle-resolved photoelectron spectrum by taking into account the initial transverse momentum distribution of photoelectrons and the focal averaging effect. Furthermore, the effect of the depletion of Ar atoms and that of the Coulombic potential originated from Ar^+ were examined. The $E_{\rm kin}$-θ asymmetry map constructed from the simulated angle-resolved photoelectron spectrum showed that a ridge structure having an almost constant phase offset of $\phi_0 \sim 90^\circ$ extends towards the larger electron kinetic-energy region above 30 eV. The results of the simulation showed that the experimental phase offset can be determined so that the ridge structure of the $E_{\rm kin}$-θ asymmetry map of the angle-resolved photoelectron spectrum takes a constant value of $\phi_0 \sim 90^\circ$.

When the peak laser field intensity is 1.2×10^{15} W/cm^2, the effect of the depletion of Ar becomes significant, and the discrepancies between the experimental and simulated angle-resolved photoelectron spectra become obvious. It was shown that the experimental $E_{\rm kin}$-$\phi_{\rm abs}$ asymmetry map and the simulated $E_{\rm kin}$-θ asymmetry map agree well with each other when the ADK rate was multiplied by a factor of 0.27.

Recent studies with elliptically polarized pulses [54,55] showed that a finite tunneling time will shift the photoelectron emission angle by a small amount. Therefore, a finite tunneling time may induce a slight uncertainty in the calibration of absolute CEP. However, the tunneling time is still a controversial research topic [56,57]. We therefore assume that the tunneling time is zero in our analysis.

The method for estimating the absolute CEP introduced in the present study will be of use for the investigation of CEP dependent ionization processes of atoms and/or molecules and dissociation processes of molecules in an intense few-cycle laser field.

ACKNOWLEDGMENTS

This work was supported by a Grant-in-Aid for Specially Promoted Research (Grants No. JP19002006 and No. JP15H05696) and a Grant-in-Aid for Scientific Research A (Grants No. JP24245003 and No. JP26288004), the Ministry of Education, Culture, Sports, Science and Technology (MEXT), Japan, JSPS through the Leading-edge Research Infrastructure Program, and a grant from the Morino Foundation for Molecular Science. G.G.P. acknowledges support from DFG (Project No. PA 730/5-1).

APPENDIX A: CTMC SIMULATION METHOD

In the simulation of the angle-resolved photoelectron spectrum, we need to take into account the distributions of $p_\perp$ and t_0. In order to estimate the number of electrons having a specific range of t_0 values, the ADK rate was calculated first using Eq. (6), because the ADK rate is considered to be proportional to the number of photoelectrons produced at $t = t_0$. Once t_0 is given, the distribution function of $p_\perp$ represented by Eq. (7) is determined, from which the number of photoelectrons having a specific range of $p_\perp$ is derived. In order to obtain $\mathbf{p}(t \to \infty)$ from Eq. (8), the two parameters t_0 and $p_\perp$ were randomly chosen so that the number of the trajectories having specific ranges of t_0 and $p_\perp$ fulfills their respective distribution functions given by Eqs. (6) and (7). In total, 20 000 000 trajectories were calculated. As the range of the time of tunneling, $-15\,\text{fs} \leqslant t_0 \leqslant +15\,\text{fs}$ is adopted. On the other hand, different ranges of the initial transverse momentum are chosen in the simulations depending on the laser field intensity. For example, the range of $-2.5\,\text{a.u.} \leqslant p_\perp \leqslant 2.5\,\text{a.u.}$ is adopted at the laser intensity of $5.1\times10^{14}\,\text{W/cm}^2$ and the range of $-3.9\,\text{a.u.} \leqslant p_\perp \leqslant 3.9\,\text{a.u.}$ is adopted at the laser intensity of $1.2\times10^{15}\,\text{W/cm}^2$.

The focal averaging is taken into account by assuming that the intensity distribution of the laser electric field around the laser propagation z axis has cylindrical symmetry. The laser electric field is described in the cylindrical coordinate system (r, z) as

$$\mathbf{E}(r,z,t) = E_0(r,z)\exp\left[-2(\ln 2)\left(\frac{t}{\Delta t}\right)^2\right]\{\hat{\mathbf{x}}'\cos[\omega t + \phi_{\text{focal}}(r,z)] - \hat{\mathbf{y}}'\sin[\omega t + \phi_{\text{focal}}(r,z)]\}. \quad \text{(A1)}$$

If the spatial profile $E_0(r,z)$ in Eq. (A1) is described by a Gaussian function as

$$E_0(r,z) = \frac{w_0}{w(z)}\exp\left[-\left(\frac{r}{w(z)}\right)^2\right], \quad \text{(A2)}$$

the CEP $\phi_{\text{focal}}(r,z)$ in Eq. (A1) is given by

$$\phi_{\text{focal}}(r,z) = -\arctan\frac{z}{z_R} + \frac{z}{z_R}\left(\frac{r}{w(z)}\right)^2, \quad \text{(A3)}$$

where

$$w(z) = w_0\sqrt{1+\left(\frac{z}{z_R}\right)^2}, \quad \text{(A4)}$$

and

$$z_R = \frac{\pi {w_0}^2}{\lambda}, \quad \text{(A5)}$$

as seen in Ref. [58].

The ionization points along the z axis, i.e., the laser propagation direction, are distributed within the spatial range of the effusive atomic beam. Because the distribution of Ar atoms around the atomic beam axis, i.e., the y axis, has cylindrical symmetry, the distribution of Ar atoms along the z axis is considered to be the same as that along the x axis. Then, the photoelectron yield was measured as a function of the focal point position along the x axis by moving the position of the focusing mirror along the x axis. The resultant distribution along the x axis can be seen as a rounded flat-top distribution whose FWHM was obtained to be 590(10) μm, which means that the FWHM along the z axis is also 590(10) μm. Therefore, the range of $-300\,\mu\text{m} \leqslant z \leqslant +300\,\mu\text{m}$ is adopted as the range of the ionization point along the z axis and the sample gas density is assumed to be uniform in this range of z in the calculation. In addition, the range of $0\,\mu\text{m} \leqslant r \leqslant 50\,\mu\text{m}$ is adopted as the range of the ionization point along the r axis.

The angle-resolved photoelectron spectrum is simulated by the trajectory calculations in which the distribution of the ionization point (r, z) is taken into account. The ionization probability $P(r,z)$ at each ionization point can be calculated by integrating the ADK rate as

$$P(r,z) = \int_{-\infty}^{\infty} W(t_0)dt_0. \quad \text{(A6)}$$

In the trajectory calculations, z and r were randomly chosen so that the number of the trajectories having specific values of z and r fulfill the distribution function of $P(r,z)2\pi r$, in which the cylindrical symmetry about the z axis is taken into account. At each ionization point (r, z), Newton's equation of motion, Eq. (8), was solved using given values of t_0 and $p_\perp$.

APPENDIX B: CTMC SIMULATION RESULT AT LOWER LASER INTENSITY

In Fig. 9, the results of the CTMC simulations performed with the laser intensity of $5.1\times10^{14}\,\text{W/cm}^2$ are shown. When the depletion effect or the Coulombic potential effect is not included, the folded E_{kin}-θ plot [Fig. 9(a)], the 3D representation of Fig. 9(a) [Fig. 9(b)], the angle-resolved photoelectron spectrum [Fig. 9(c)], and the E_{kin}-θ asymmetry map constructed from Fig. 9(c) [Fig. 9(d)] are obtained.

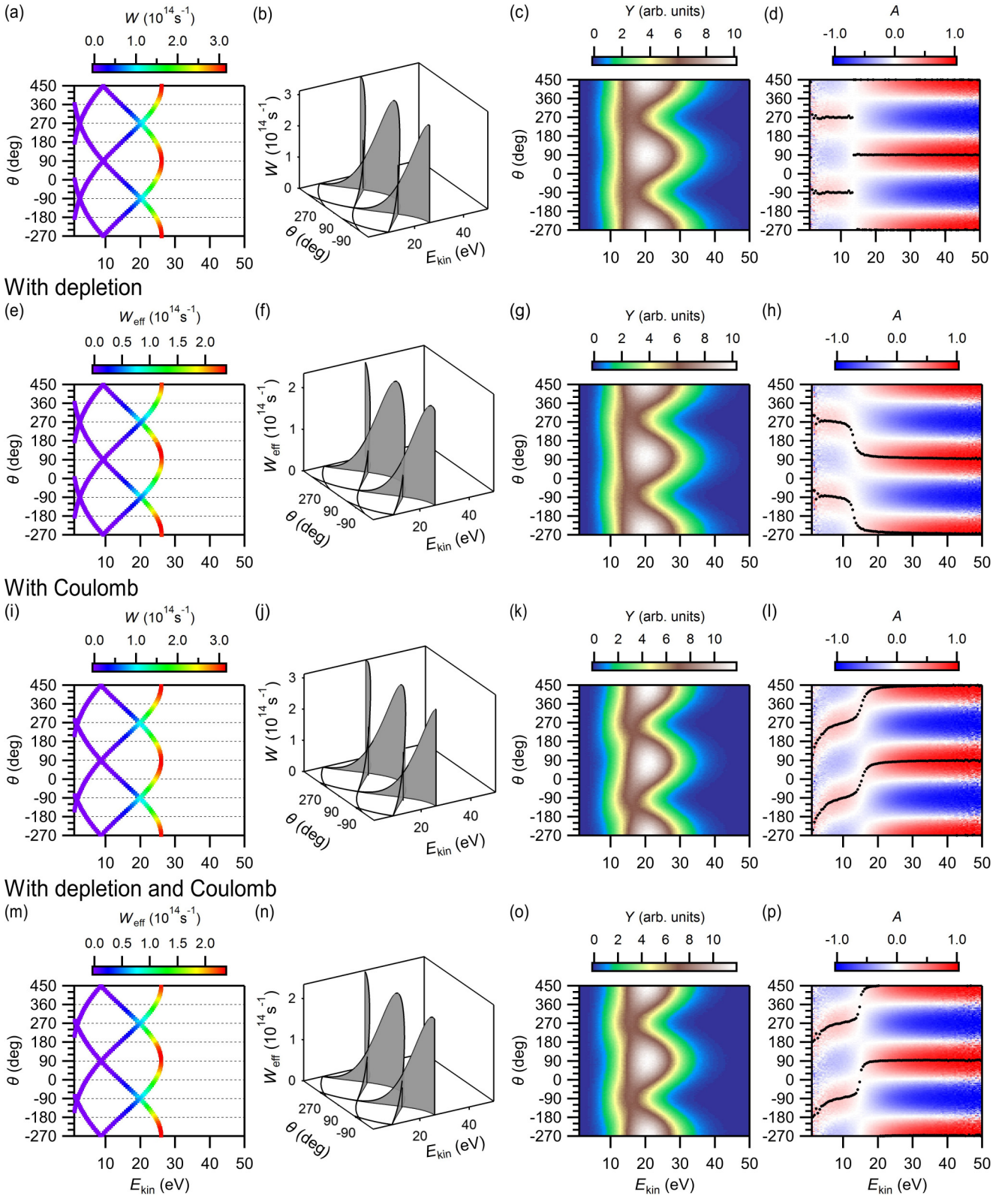

FIG. 9. The results of the CTMC simulations obtained when the peak laser intensity is 5.1×10^{14} W/cm^2. The folded $E_{\rm kin}$-θ plot, their 3D representations, the corresponding angle-resolved photoelectron spectra, and the corresponding $E_{\rm kin}$-θ asymmetry maps are shown. The top row for (a)–(d) shows the results obtained when neither the effect of the depletion of neutral Ar nor that of the Coulomb potential of Ar^+ is taken into account. The second row for (e)–(h) shows the results obtained when only the effect of the depletion of neutral Ar is taken into account. The third row for (i)–(l) shows the results obtained when only the effect of the Coulomb potential of Ar^+ is taken into account. The bottom row for (m)–(p) shows the results obtained when both of the two effects are taken into account.

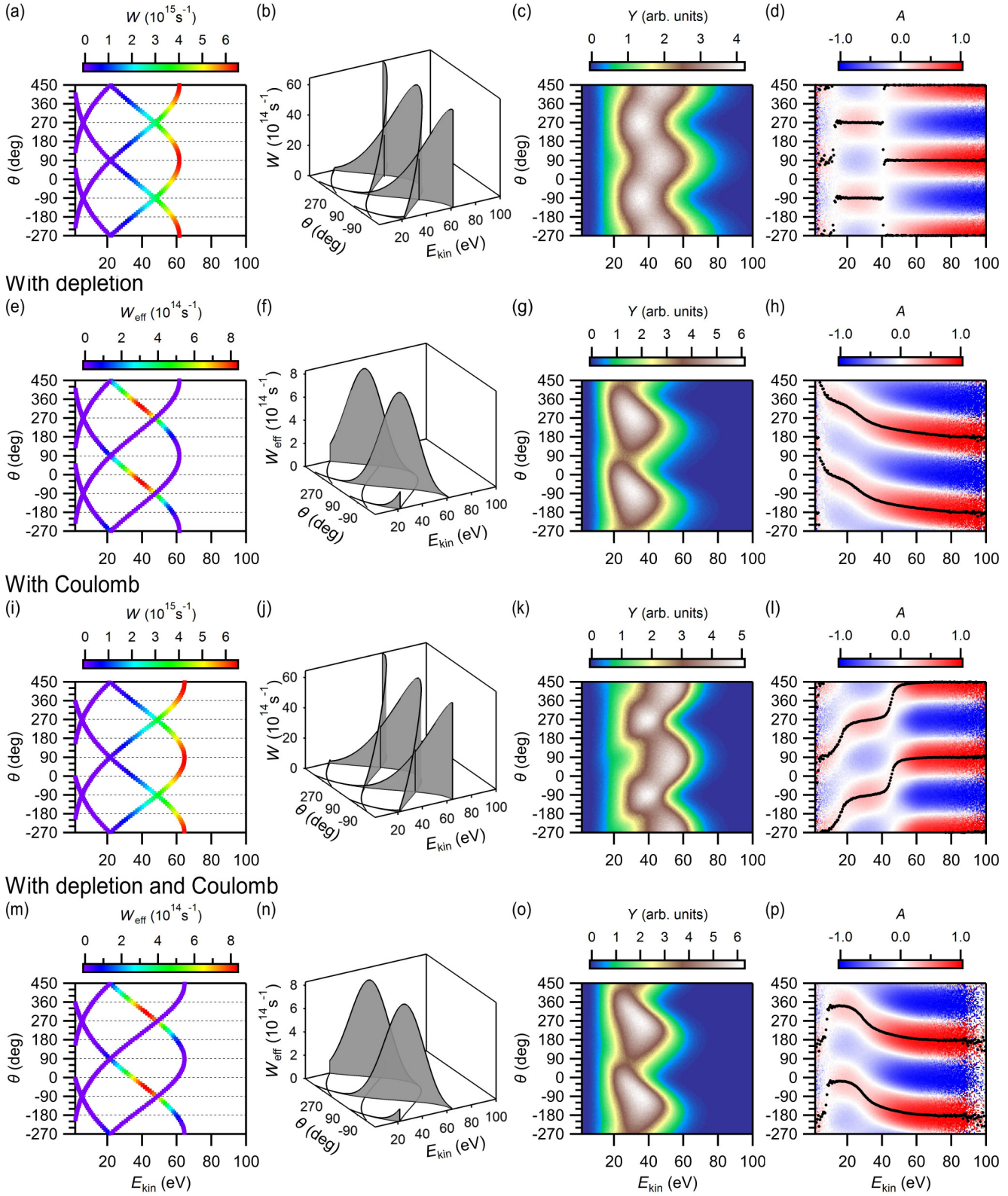

FIG. 10. The results of the CTMC simulations obtained when the peak laser intensity is 1.2×10^{15} W/cm^2. The folded $E_{\rm kin}$-θ plot, their 3D representations, the corresponding angle-resolved photoelectron spectra, and the corresponding $E_{\rm kin}$-θ asymmetry maps are shown. The top row for (a)–(d) shows the results obtained when neither the effect of the depletion of neutral Ar nor that of the Coulomb potential of Ar^+ is taken into account. The second row for (e)–(h) shows the results obtained when only the effect of the depletion of neutral Ar is taken into account. The third row for (i)–(l) shows the results obtained when only the effect of the Coulomb potential of Ar^+ is taken into account. The bottom row for (m)–(p) shows the results obtained when both of the two effects are taken into account.

When only the depletion of neutral Ar is taken into account, Figs. 9(a)–9(d) are converted into Figs. 9(e)–9(h), respectively. When only the Coulombic potential of Ar^+ is taken into account, Figs. 9(a)–9(d) are converted into Figs. 9(i)–9(l), respectively. When both the depletion of neutral Ar and the Coulombic potential of Ar^+ are taken into account, Figs. 9(a)–9(d) are converted into Figs. 9(m)–9(p), respectively.

APPENDIX C: CTMC SIMULATION RESULT AT HIGHER LASER INTENSITY

In Fig. 10, the results of the CTMC simulations performed with the laser intensity of $1.2\times10^{15}\,\mathrm{W/cm^2}$ are shown. When the depletion effect or the Coulombic potential effect is not included, the folded E_{kin}-θ plot [Fig. 10(a)], the 3D representation of Fig. 10(a) [Fig. 10(b)], the angle-resolved photoelectron spectrum [Fig. 10(c)], and the E_{kin}-θ asymmetry map constructed from Fig. 10(c) [Fig. 10(d)] are obtained. As can be seen in Fig. 10(d), the obtained phase offset takes an almost constant value of $\phi_0 \sim 90^\circ$ in the range of $E_{\mathrm{kin}} > 45\,\mathrm{eV}$.

When only the depletion of neutral Ar is taken into account, Figs. 10(a)–10(d) are converted into Figs. 10(e)–10(h), respectively. The phase offset shown in Fig. 10(d) monotonically decreases as E_{kin} increases, exhibiting the strong depletion effect. When only the Coulombic potential of Ar^+ is taken into account, Figs. 10(a)–10(d) are converted into Figs. 10(i)–10(l), respectively. The phase offset increases as E_{kin} increases and takes an almost constant value of $\phi_0 \sim 90^\circ$ in the range of $E_{\mathrm{kin}} > 80\,\mathrm{eV}$, similar to the behavior shown in Fig. 6(h), obtained at the lower laser intensity of $5.1\times10^{14}\,\mathrm{W/cm^2}$. When both the depletion of neutral Ar and the Coulombic potential of Ar^+ are taken into account, Figs. 10(a)–10(d) are converted into Figs. 10(m)–10(p), respectively.

[1] M. Nisoli, S. De Silvestri, and O. Svelto, Appl. Phys. Lett. **68**, 2793 (1996).

[2] G. G. Paulus, F. Lindner, H. Walther, A. Baltuška, E. Goulielmakis, M. Lezius, and F. Krausz, Phys. Rev. Lett. **91**, 253004 (2003).

[3] N. A. Papadogiannis, B. Witzel, C. Kalpouzos, and D. Charalambidis, Phys. Rev. Lett. **83**, 4289 (1999).

[4] P. B. Corkum and F. Krausz, Nat. Phys. **3**, 381 (2007).

[5] A. Baltuška, T. Udem, M. Uiberacker, M. Hentschel, E. Goulielmakis, C. Gohle, R. Holzwarth, V. S. Yakovlev, A. Scrinzi, T. W. Hansch, and F. Krausz, Nature (London) **421**, 611 (2003).

[6] P. Dietrich, F. Krausz, and P. B. Corkum, Opt. Lett. **25**, 16 (2000).

[7] G. G. Paulus, F. Grasbon, H. Walther, P. Villoresi, M. Nisoli, S. Stagira, E. Priori, and S. De Silvestri, Nature (London) **414**, 182 (2001).

[8] M. F. Kling, C. Siedschlag, A. J. Verhoef, J. I. Khan, M. Schultze, T. Uphues, Y. Ni, M. Uiberacker, M. Drescher, F. Krausz, and M. J. J. Vrakking, Science **312**, 246 (2006).

[9] X. Xie, K. Doblhoff-Dier, S. Roither, M. S. Schöffler, D. Kartashov, H. Xu, T. Rathje, G. G. Paulus, A. Baltuška, S. Gräfe, and M. Kitzler, Phys. Rev. Lett. **109**, 243001 (2012).

[10] S. Miura, T. Ando, K. Ootaka, A. Iwasaki, H. Xu, T. Okino, K. Yamanouchi, D. Hoff, T. Rathje, G. G. Paulus, M. Kitzler, A. Baltuška, G. Sansone, and M. Nisoli, Chem. Phys. Lett. **595–596**, 61 (2014).

[11] A. S. Alnaser, M. Kübel, R. Siemering, B. Bergues, N. G. Kling, K. J. Betsch, Y. Deng, J. Schmidt, Z. A. Alahmed, A. M. Azzeer, J. Ullrich, I. Ben-Itzhak, R. Moshammer, U. Kleineberg, F. Krausz, R. de Vivie-Riedle, and M. F. Kling, Nat. Commun. **5**, 3800 (2014).

[12] M. Kübel, R. Siemering, C. Burger, N. G. Kling, H. Li, A. S. Alnaser, B. Bergues, S. Zherebtsov, A. M. Azzeer, I. Ben-Itzhak, R. Moshammer, R. de Vivie-Riedle, and M. F. Kling, Phys. Rev. Lett. **116**, 193001 (2016).

[13] H. Yazawa, T. Shioyama, Y. Suda, F. Kannari, R. Itakura, and K. Yamanouchi, J. Chem. Phys. **125**, 184311 (2006).

[14] R. Itakura, P. Liu, Y. Furukawa, T. Okino, K. Yamanouchi, and H. Nakano, J. Chem. Phys. **127**, 104306 (2007).

[15] H. Xu, T. Okino, T. Kudou, K. Yamanouchi, S. Roither, M. Kitzler, A. Baltuška, and S. L. Chin, J. Phys. Chem. A **116**, 2686 (2012).

[16] C. A. Haworth, L. E. Chipperfield, J. S. Robinson, P. L. Knight, J. P. Marangos, and J. W. G. Tisch, Nat. Phys. **3**, 52 (2007).

[17] R. Kienberger, E. Goulielmakis, M. Uiberacker, A. Baltuška, V. Yakovlev, F. Bammer, A. Scrinzi, T. Westerwalbesloh, U. Kleineberg, U. Heinzmann, M. Drescher, and F. Krausz, Nature (London) **427**, 817 (2004).

[18] X. Liu, H. Rottke, E. Eremina, W. Sandner, E. Goulielmakis, K. O. Keeffe, M. Lezius, F. Krausz, F. Lindner, M. G. Schätzel, G. G. Paulus, and H. Walther, Phys. Rev. Lett. **93**, 263001 (2004).

[19] N. G. Johnson, O. Herrwerth, A. Wirth, S. De, I. Ben-Itzhak, M. Lezius, B. Bergues, M. F. Kling, A. Senftleben, C. D. Schröter, R. Moshammer, J. Ullrich, K. J. Betsch, R. R. Jones, A. M. Sayler, T. Rathje, K. Rühle, W. Müller, and G. G. Paulus, Phys. Rev. A **83**, 013412 (2011).

[20] P. B. Corkum, Phys. Rev. Lett. **71**, 1994 (1993).

[21] G. G. Paulus, W. Becker, W. Nicklich, and H. Walthe, J. Phys. B: At. Mol. Opt. Phys. **27**, L703 (1994).

[22] A. M. Sayler, M. Arbeiter, S. Fasold, D. Adolph, M. Möller, D. Hoff, T. Rathje, B. Fetić, D. B. Milošević, T. Fennel, and G. G. Paulus, Opt. Lett. **40**, 3137 (2015).

[23] B. Bergues, Opt. Exp. **20**, 25317 (2012).

[24] A. I. Titov, B. Kämpfer, A. Hosaka, T. Nousch, and D. Seipt, Phys. Rev. D **93**, 045010 (2016).

[25] P. L. He, C. Ruiz, and F. He, Phys. Rev. Lett. **116**, 203601 (2016).

[26] C. P. J. Martiny and L. B. Madsen, Phys. Rev. Lett. **97**, 093001 (2006).

[27] C. P. J. Martiny and L. B. Madsen, Phys. Rev. A **76**, 043416 (2007).

[28] K. J. Yuan, S. Chelkowski, and A. D. Bandrauk, Phys. Rev. A **93**, 053425 (2016).

[29] M. Bashkansky, P. H. Bucksbaum, and D. W. Schumacher, Phys. Rev. Lett. **60**, 2458 (1988).

[30] S. Basile, F. Trombetta, and G. Ferrante, Phys. Rev. Lett. **61**, 2435 (1988).

[31] A. Jaroń, J. Z. Kamiński, and F. Ehlotzky, Opt. Commun. **163**, 115 (1999).
[32] S. P. Goreslavski, G. G. Paulus, S. V. Popruzhenko, and N. I. Shvetsov-Shilovski, Phys. Rev. Lett. **93**, 233002 (2004).
[33] C. P. J. Martiny, M. Abu-Samha, and L. B. Madsen, J. Phys. B: At. Mol. Opt. Phys. **42**, 161001 (2009).
[34] ALPHA5000, Thales.
[35] PC70 and PC52, Ultrafast Innovations.
[36] OA513, FemtoOptics.
[37] F. Silva, M. Miranda, B. Alonso, J. Rauschenberger, V. Pervak, and H. Crespo, Opt. Exp. **22**, 10181 (2014).
[38] T. Wittmann, B. Horvath, W. Helml, M. G. Schätzel, X. Gu, A. L. Cavalieri, G. G. Paulus, and R. Kienberger, Nat. Phys. **5**, 357 (2009).
[39] ARTOF-10k, VG Scienta.
[40] J. R. Birge, R. Ell, and F. X. Kärtner, Opt. Lett. **31**, 2063 (2006).
[41] J. R. Birge, H. M. Crespo, and F. X. Kärtner, J. Opt. Soc. Am. B-Opt. Phys. **27**, 1165 (2010).
[42] OA229, FemtoOptics.
[43] DLD40, Roentdek.
[44] IUC-130CN3, Trinity.
[45] DP1400, Agilent Technologies.
[46] A. M. Perelomov and V. S. Popov, Sov. Phys. JETP **25**, 336 (1967).
[47] M. V. Ammosov, N. B. Delone, and V. P. Krainov, Sov. Phys. JETP **64**, 1191 (1986).
[48] P. Eckle, M. Smolarski, P. Schlup, J. Biegert, A. Staudte, M. Schöffler, H. G. Muller, R. Dörner, and U. Keller, Nat. Phys. **4**, 565 (2008).
[49] N. B. Delone and V. P. Krainov, J. Opt. Soc. Am. B **8**, 1207 (1991).
[50] A. N. Pfeiffer, C. Cirelli, M. Smolarski, D. Dimitrovski, M. Abu-samha, L. B. Madsen, and U. Keller, Nat. Phys. **8**, 76 (2011).
[51] N. I. Shvetsov-Shilovski, D. Dimitrovski, and L. B. Madsen, Phys. Rev. A **85**, 023428 (2012).
[52] T. Otobe and K. Yabana, Phys. Rev. A **75**, 062507 (2007).
[53] L. V. Keldysh, Sov. Phys. JETP **20**, 1307 (1965).
[54] P. Eckle, A. N. Pfeiffer, C. Cirelli, A. Staudte, R. Dörner, H. G. Muller, M. Büttiker, and U. Keller, Science **322**, 1525 (2008).
[55] A. S. Landsman, M. Weger, J. Maurer, R. Boge, A. Ludwig, S. Heuser, C. Cirelli, L. Gallmann, and U. Keller, Optica **1**, 343 (2014).
[56] L. Torlina, F. Morales, J. Kaushal, I. Ivanov, A. Kheifets, A. Zielinski, A. Scrinzi, H. G. Muller, S. Sukiasyan, M. Ivanov, and O. Smirnova, Nat. Phys. **11**, 503 (2015).
[57] N. Teeny, E. Yakaboylu, H. Bauke, and C. H. Keitel, Phys. Rev. Lett. **116**, 063003 (2016).
[58] R. W. Boyd, J. Opt. Soc. Am. **70**, 877 (1980).